ELSEVIER

Contents lists available at ScienceDirect

Photonics and Nanostructures - Fundamentals and Applications

journal homepage: www.elsevier.com/locate/photonics





Broadband characterization of the spectral responsivity of thermoelectrically-coupled nanoantennas

Chao Dong ^{a,b,*}, Gergo P. Szakmany ^b, Hadrian Aquino ^b, Wolfgang Porod ^b, Alexei O. Orlov ^b, Edward C. Kinzel ^{b,c}, Gary H. Bernstein ^b, David Burghoff ^{a,b}

- ^a Department of Electrical and Computer Engineering, Austin, TX, USA
- ^b Department of Electrical Engineering, Notre Dame, IN, USA
- ^c Department of Aerospace and Mechanical Engineering, Notre Dame, IN, USA

ARTICLE INFO

Keywords.

Mid-wave and long-wave infrared detection Thermoelectrically coupled nanoantennas Nanoantenna-enhanced IR spectroscopy *PACS*: 00.00.00

ABSTRACT

Thermoelectrically-coupled nanoantennas (TECNAs)—nanoantennas that use the Seebeck effect to detect radiation—are a promising modality for spectrally resolved detection in the infrared. By tailoring the geometry of a nanoantenna coupled to a micro-cavity, their responsivity and spectral selectivity can be carefully designed. However, to date no measurements have directly established the spectral response of these detectors over a large frequency span in the infrared regime, particularly from 2 μ m to 20 μ m. In this work, we provide a comprehensive analysis of the spectral selectivity of TECNAs operating within the mid- and long-wave infrared (MWIR and LWIR) regions. We engineer arrays of detectors at 5.5 μ m, 10.6 μ m, and 14 μ m, and we verify their selectivity using polarization-dependent Fourier-transform infrared spectroscopy (FTIR). We also show that the response can be tailored using a combination of antenna and cavity design. Our results not only underscore the potential of TECNAs in advancing sensing applications within the MWIR and LWIR domains, but also offer a promising direction for enhancing other detector modalities.

1. Introduction

In recent years, infrared (IR) technology has seen notable advancements, becoming increasingly relevant across sectors including science [1], industry [2], and medicine [3]. While the short-wave infrared (SWIR) spectrum has been a focal point of research, the MWIR and LWIR spectra hold untapped potential that could be impactful for a range of applications. However, detection in the MWIR and LWIR ranges presents unique challenges, primarily due to device-oriented factors such as thermal noise [4], pixel pitch limitations [5], and integration complexities [6]. A number of detector modalities have been created, with DTGS and HgCdTe being especially popular due to their capability to generate strong signals even under low-flux conditions [7]. However, these detectors present challenges due to their relatively large size. In particular, HgCdTe is typically cooled for optimum performance. Recently, the spotlight has shifted to microbolometers as potential solutions for chip-scale infrared detection. While they offer several advantages and can be readily turned into focal plane arrays, they require regular calibration to counteract noise and may have specific operational temperature range limitations [7]. Quantum well infrared photodetectors (QWIPs) have also emerged as prominent players in infrared detection, with designs targeting chip-scale integration. Renowned for their wavelength selectivity, thermal stability, and high responsivity and detectivity, QWIPs, however, face challenges such as expensive material growth over large areas [8]. Additionally, infrared dipole antennas have been integral to IR detection for decades, primarily focusing on tailoring antenna dimensions for optimal response at specific, fixed wavelengths [9]. This method, while effective for targeted wavelengths, does not employ a broad light source for characterization, limiting the scope of spectral analysis. Consequently, the peak wavelength where a given antenna exhibits its strongest signal remains unclear, and one cannot assess its broadband response directly.

TECNAs [10–12] are promising alternatives that could allow for the creation of versatile frequency-selective detectors. By confining the field into a nanoscale volume and using the thermoelectric (Seebeck) effect to detect local heating, these nanoantennas offer a mechanism for converting radiation-induced currents into electrical signals, providing frequency selectivity without the bulk and cooling requirements of

^{*} Corresponding author at: Department of Electrical and Computer Engineering, University of Texas at Austin, Austin, TX, USA. *E-mail address:* chaodong@utexas.edu (C. Dong).

traditional systems [13]. Moreover, the incorporation of these nanoantennas into compact photonic systems could aid their integration in miniaturized, efficient, and adaptable infrared sensing devices, which can be used in a variety of frequency bands [14–22]. However, though these TECNAs have been extensively characterized in terms of responsivity, speed, and noise performance, their spectral dependence has not been measured or exploited.

In this work, we perform the first measurement of the spectral dependence of TECNA detectors. We fabricate arrays of nanoantennas by depositing Pd and Ni on intrinsic silicon (Si) and employing an etching technique to suspend them. Beneath the TECNA, a quasihemispherical cavity provides thermal insulation. This cavity also possesses reflective properties, acting as focusing back-reflector that increases the interaction between the IR light and the nanoantenna. By adjusting the dimensions of our cavity and antenna, we design antennas of different resonant frequencies and assess their responsivity using FTIR. By illuminating the TECNA with an infrared glowbar and recording the detected signal as the interferometer scans, we are able to record detectivity spectra that distinctly highlight the TECNAs' designed spectral selectivity at 5.5 µm, 10.6 µm, and 14 µm. Polarizationdependent measurements for the 5.5 µm design further validate the pronounced spectral selectivity inherent in the TECNAs, and our results agree well with simulations.

2. Results

2.1. Device overview and design

The basic concept of TECNAs is highlighted in Fig. 1. They are fabricated through a combination of micro- and nano-fabrication

techniques—details of the fabrication process can be found in a previous publication [23]. A schematic representation of TECNAs is shown in Fig. 1a. IR light is focused onto the antenna, and for light with a wavelength that matches the antenna's design, localized heating is generated inside the metallic antenna structure and at the end of the lead structure. These lead lines are pivotal for the thermocouple formation, as the junction between them acts as a hot junction and allows the detection of radiation. They also contribute resistance, Johnson noise, and mechanical stress. The nanothermocouple then converts the nanoantenna's heat into voltage, leveraging the Seebeck effect [24] to produce a voltage at the resonant wavelength. The whole TECNA is typically suspended over a cavity, which not only offers thermal insulation but also plays a crucial role in enhancing the device's optical absorption. The cold junctions of the thermocouple are located tens of microns away from the hot junction, outside the range of the antenna heating. They are situated on the Si substrate, where the leads of the thermocouple overlap with the bonding pads. The thermal conductivity of the Si substrate is 139 W m⁻¹ K⁻¹, and it acts as a very efficient heat sink, maintaining the temperature of the cold junctions consistently at room temperature.

The SEM image in Fig. 1b provides a detailed view of an individual TECNA, emphasizing its antenna, lead lines, and cavity. The design of the devices' parameters was determined by our previous work. We used COMSOL to find the right antenna length and width [10,25] and cavity size [26] for a given wavelength. In these simulations, we focused on maximizing the temperature increase at the center of the dipole, aligning the design with the operational wavelength. The schematic in Fig. 1a elaborates on the parameters and thicknesses of the antenna and lead lines. We have designed three configurations: $5.5~\mu m$, $10.6~\mu m$, and $14~\mu m$. The specific parameters for the antenna and cavity of these designs

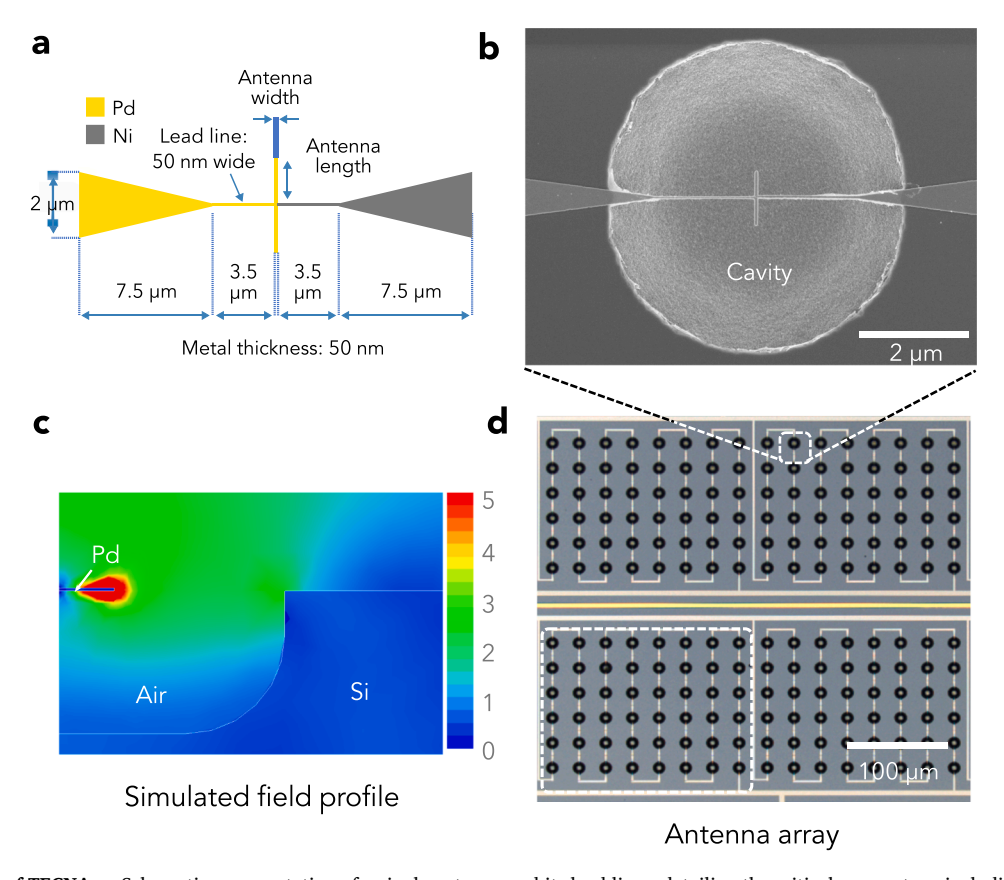


Fig. 1. Basic concept of TECNAs.a Schematic representation of a single antenna and its lead lines, detailing the critical parameters, including the thickness of the antenna and lead lines. b SEM image of a single TECNA, displaying the antenna, lead lines, and cavity. c HFSS simulation showing the field around the nanoantenna, highlighting the regions of intense electromagnetic interaction. d Optical microscope image showcasing four arrays of nanoantennas. The rectangular outline highlights one array containing 48 TECNAs.

Table 1Design Parameters of the TECNAs.

λ (μm)	Width (nm)	Length (µm)	Diameter (µm)	Height (μm)
5.5	90	1.9	7.8	2.5
10.6	100	3.9	9.2	2.7
14	120	5.9	17.3	4.9

are detailed in Table 1. The quasi-hemispherical shape of the cavity acts like a dish reflector, creating interference between the incident and reflected IR waves, thereby intensifying the interaction between the IR light and the nanoantenna. This geometry ensures effective capture and concentration of waves from the glowbar onto the nanoantenna. Additionally, the cavity design helps in retaining the heat locally, ensuring that the heat is efficiently converted into voltage by the nanothermocouple without being lost to the surroundings.

Based on the physical apertures of our TECNAs, which range from 8 μm to 17 μm and are designed to resonate at center wavelengths of 5.5 μm , 10.6 μm , and 14 μm , the calculated effective areas are 48 μm^2 , 66 μm^2 , and 232 μm^2 , respectively. These relatively small effective areas indicate that performance can be significantly enhanced by processing the TECNAs into arrays. Fig. 1d displays an optical microscope image of four nanoantenna arrays, each consisting of N TECNAs connected in series through cold junctions. In thermoelectric devices, the cold junction serves as a reference, ensuring a consistent baseline for the temperature difference experienced at the hot junctions. By connecting N detectors in series, the output voltage increases linearly by a factor of N, while the Johnson noise power also increases proportionally. Consequently, the signal-to-noise ratio improves by a factor of \sqrt{N} , enhancing the overall detection capability of the array.

The most important component of the TECNA's operation is the hot junction, located in the center of Fig. 1b. This junction, emerging at the confluence of the antenna and lead lines, serves as the focal point for converting heat into voltage. When the antenna is heated by incident radiation, it leverages the difference in Seebeck coefficients between Pd and Ni. This difference generates an open-circuit voltage, $V_{\rm OC}$, which is proportional to the temperature difference between the hot and cold junctions. The relationship is given by $V_{\rm OC} = \Delta S(T_a - T_0)$, where $V_{\rm OC}$ denotes the open-circuit voltage produced by the thermopile, ΔS represents the relative Seebeck coefficient for the Pd-Ni junction (8.9 μ V K $^{-1}$ [27] for the Ni/Pd combination), and T_a and T_0 correspond to the temperatures of the antenna and substrate, respectively.

As TECNAs have a complex design space, including a dipole antenna, cavity, and lead lines, detailed analysis of their electromagnetic properties requires accurate simulation. For this analysis, we used the High-Frequency Structure Simulator (HFSS) to perform a full-wave frequency domain finite element analysis (FEA). The TECNA's representation in HFSS is shown in Fig. 1c, while Fig. 1a gives a closer view of the lead lines, highlighting the parameters important for our simulations. One of the TECNA's key features is its quasi-hemispherical cavity, which is hemispherical on the sides and flat on the bottom—this oblong shape was rendered in our simulations to maximize the accuracy. The power absorbed by the antenna from incident radiation is described in terms of the incident irradiation power density, providing an effective aperture area.

In our simulations, we use radiation boundary conditions and exploit the symmetry of the system. As the dimensions of typical TECNA cavities are on the order of a wavelength, we exposed them to an incident plane wave, which is accurate even for fairly tightly-focused beams. The interaction between this wave and the TECNA produces a radiation pattern that helps us to understand the TECNA's electromagnetic responses. As shown in Fig. 1c, the simulations display strong field enhancement around the nanoantenna, offering insights into the design details of the nanoantenna and how it interacts with incident IR radiation. Additionally, the simulations included calculating the ratio of incident radiation absorbed by the antenna to the total incident

radiation, providing an accurate evaluation of the TECNAS' responsivity.

To improve the accuracy of our simulations, we took the shapes of the dipole nanoantenna and the lead lines directly from our fabricated devices, as seen in Fig. 1a, verified using SEM. Table 1 provides more information on the specific parameters and dimensions central to our TECNA designs, especially those related to the antenna and cavity. The simulations highlight areas with intense electromagnetic interactions, confirming the efficiency of the TECNA's design in the IR range.

2.2. Optical setup and measurements

The spectrum of our TECNAs were measured using a Bruker 70 V FTIR system. This system is configured conventionally with a Michelson interferometer, as depicted in Fig. 2a. The light source, a glowbar, emitted a collimated beam covering a spectral range from 4 µm to 25 μm. This beam traversed the FTIR and was subsequently focused onto the nanoantenna using an off-axis parabolic (OAP) mirror with a 4-inch focal length. Since the thermocouple junction could also capture unwanted photocurrent from near-infrared light impinging on the Si, we placed a 2 mm germanium (Ge) crystal in front of the nanoantenna to filter out detection of wavelengths shorter than 2 µm. The focus of our FTIR measurements is on capturing the TECNAs' response to the infrared radiation emitted by the glowbar, which is based on the temperature differential generated between the hot and cold junctions. This measurement approach effectively avoids the appearance of element signals like Si, palladium, or nickel in the spectra, as it prioritizes the detection of thermal effects at the nanoantennas over the elemental absorbance spectra.

Because the noise equivalent power (NEP) of our system was approximately $4.5\times~10^{-10}~W/\sqrt{Hz}$, we used our FTIR in step-scan mode, which stops the interferometer during data acquisition. This

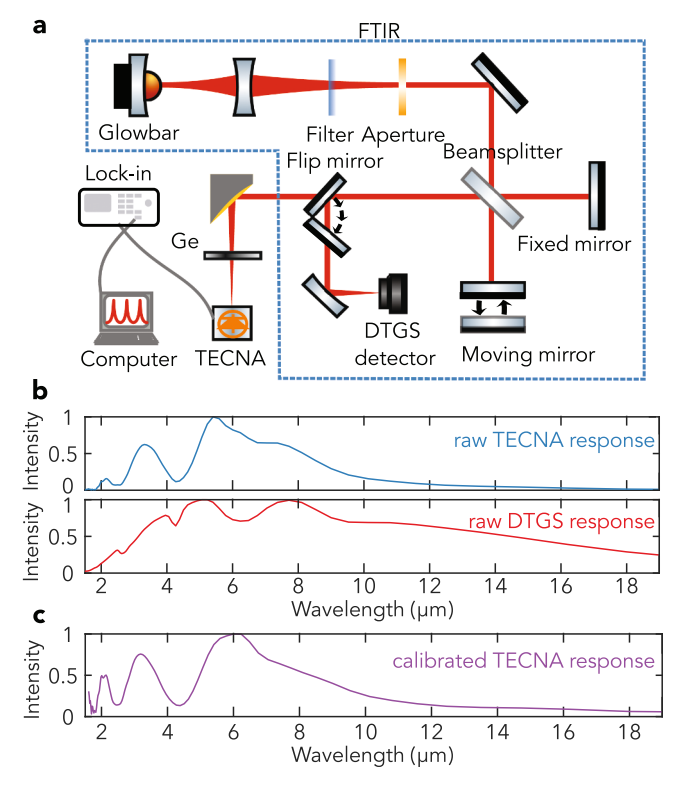


Fig. 2. Experimental setup and basic results.a Comprehensive schematic illustrating the optical components and their arrangement in the TECNA characterization. b Raw response spectrum of the TECNA tailored for 5.5 μ m, contrasted with the DTGS detector's response. c Calibrated responsivity curve of the TECNA, demonstrating its peak performance around 6 μ m.

allowed us to improve the temporal resolution and optimize the signal-to-noise ratio with a long time constant (10 s). By acquiring interferograms at distinct intervals across the delay line, the step-scan method allows for a precise reconstruction of the TECNA response. To collect a spectroscopic reference, we used the FTIR's internal DTGS detector. Fig. 2b shows the resulting spectra. The upper (blue) curve represents the raw TECNA response, while the lower (red) curve illustrates the raw data from the DTGS detector, capturing the detectivity of the DTGS detector and the inherent spectral characteristics of the glowbar's emission. A flip mirror is used to facilitate switching the glowbar's light between the TECNA and the internal DTGS detector.

The calibration of the TECNA's response involves a two-step process. Initially, we normalize the raw TECNA data using the raw DTGS response to account for the spectral properties of the glowbar. This step ensures that the TECNA's response remains free from bias introduced by the glowbar's emission profile. Subsequently, the normalized data undergoes a correction based on the detectivity (D^*) of the DTGS detector, which varies with frequency, as detailed in reference [28]. The culmination of this calibration process yields the final TECNA response, as showcased in Fig. 2c.

While the setup described above was adequate for standard measurements, experiments involving polarized light required the integration of a ZnSe holographic wire grid polarizer placed in front of the Ge crystal. This configuration enabled the measurement of both co- and cross-polarization measurements. In this context, "co-polarization" signifies that the light's polarization direction aligns with the antenna's orientation after passing through the polarizer, while "cross-polarization" refers to the condition where the polarization direction is perpendicular to the antenna, aligning with the feed, as demonstrated in Fig. 1a.

Figure 3 presents a comprehensive comparison of the different TECNAs' responsivities. Figs. 3a-c display both experimental measurements (in blue) and HFSS simulations (in red) for the respective TECNA designs. Specifically, Figs. 3a-c depict the calibrated responsivity for the 5.5 $\mu m,~10.6~\mu m,~and~14~\mu m$ designs. Each of the antennas displays a common behavior: a strong peak at the design frequency, along with a

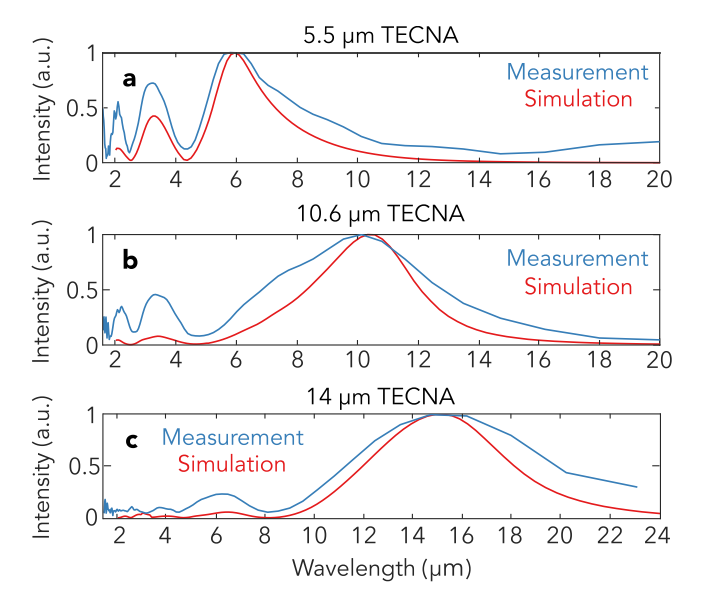


Fig. 3. TECNA measurements and simulations.a Calibrated responsivity for the 5.5 μm TECNA design. Blue represents experimental data (determined using the calibration procedure discussed in Fig. 2), and red indicates HFSS simulations (determined by comparing the power absorbed in the antenna to the incident power). Both have been normalized such that their peak value is defined to be 1. b Calibrated responsivity for the 10.6 μm TECNA design. c Calibrated responsivity for the 14 μm TECNA design.

Table 2Comparison of primary and secondary peak positions from HFSS simulations and experimental evaluations for various TECNA designs.

Design & Condition	Data Source	Main Peak (μm)	Side Peak (μm)
5.5 μm	HFSS	5.8	3.3
	Experiment	5.9	3.2
10.6 μm	HFSS	10.7	3.5
	Experiment	10.1	3.6
14 μm	HFSS	15.0	6.5
	Experiment	14.7	6.3
5.5 μm (Co-pol.)	HFSS	5.9	3.3
	Experiment	5.7	3.2
5.5 μm (Cross-pol.)	HFSS	7	3.2
	Experiment	7.7	3.1

series of increasingly weak peaks at higher frequencies. Notably, both the experimental and simulated data are presented as dimensionless quantities, thus intensity (in arbitrary units) is used to represent the responsivity for each design.

Good agreement is observed between the TECNA responses obtained from HFSS simulations and the ones obtained from experimental measurements. Table 2b compares the nanoantenna responsivity from measurements and simulations. The close alignment of peak positions between the HFSS simulation results and our experimental measurements validates the design's spectral selectivity, underscoring the nanoantenna's significant role in enhancing responsivity. However, some differences are notable. For example, the experimental data has a broader main peak and increased response at shorter wavelengths in the measurements compared to the HFSS predictions. This can be attributed to the differences in the light sources used. Our experimental measurements employed an unpolarized glowbar that covers a wide polarization spectrum. In contrast, the HFSS simulations were based on a polarized plane wave. The inherent nature of an unpolarized source means it encompasses an incoherent mixture of both possible polarizations. While nanoantennas are primarily sensitive to polarizations that align with their orientation, the cross-polarization is still focused by the cavity and can be subsequently detected by the nanoantennas. This accounts for the difference in the two results.

3. Discussion

In order to account for the discrepancies between measurement and simulation, polarization-dependent measurements were performed. While both polarizations can be absorbed in the lead lines, only copolarized light will be efficiently absorbed in the antenna. This breaks the symmetry between the two polarizations. Fig. 4a further explores the co-polarization and cross-polarization responsivity of the 5.5 µm TECNA, with an inset illustrating the responsivity against frequency in terahertz (THz). As observed in Fig. 3a, the responsivity of the 5.5 μm TECNA with unpolarized light displays a distinct 'tail' emerging on the longer-wavelength side (beyond 7 μ m). This feature is further corroborated by the polarization-dependent measurements in Fig. 4a. In the copolarization measurement, the 'tail' is notably diminished, and the measurement agrees almost exactly with the simulation. However, in the cross-polarization measurement, the peak shifts to around 7.5 μm, as predicted by theory. This underscores the effect of the antenna in shaping the responsivity. The co-polarization measurements, benefiting from the nanoantenna's enhancement, exhibit a much stronger signal compared to their cross-polarization counterparts. This result is in very good agreement with theory. However, the cross-polarization measurements, especially below 5 µm, are much weaker, and as a result have much greater discrepancy to theory. The fact that the secondary peak near 3 μm is considerably stronger likely implicates scattering as the explanation for the discrepancy. As the cavities are not perfectly optically smooth, scattering can convert the cross- to co-polarization light, an effect that would be expected to be more pronounced at shorter

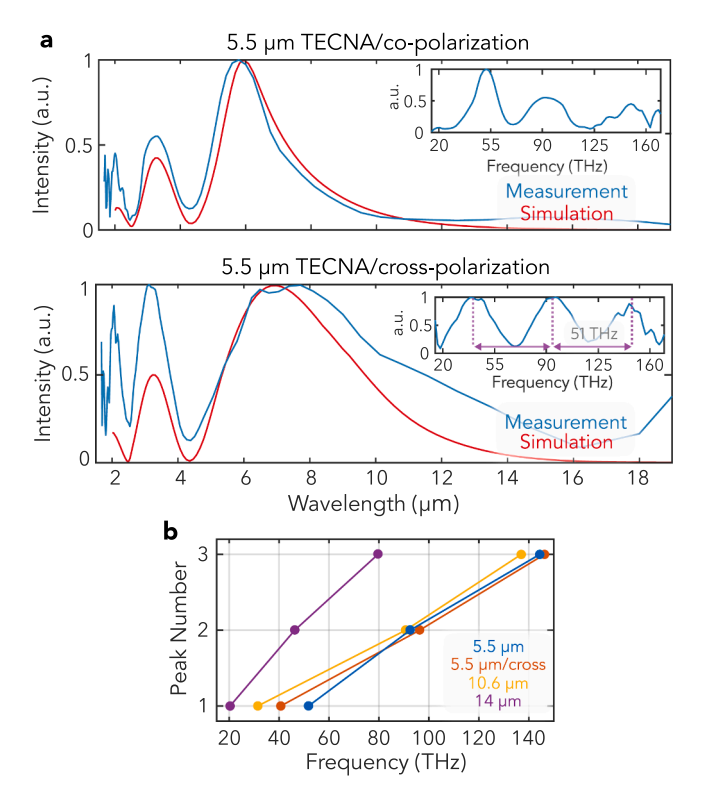


Fig. 4. TECNA measurements and simulations.a Co-polarization and cross-polarization responsivity of the 5.5 μm TECNA. Blue curves indicate experimental data and red curves represent HFSS simulations. An inset shows the responsivity with intensity versus Frequency (THz). **b** Peak number versus frequency for TECNA designs. Data points are derived from experimental results in Fig. 3 and 4. Colors indicate different TECNA designs.

wavelengths.

Next, we examine the origin of the various peaks and of the spectral selectivity. Fig. 4b charts peak number versus frequency, converting peak positions from wavelength to frequency. In Fig. 4a, the inset provides a detailed view of responsivity as a function of frequency. The cross-polarization inset for the 5.5 μ m design displays a uniformly spaced spectrum. In contrast, the co-polarization inset of the same design reveals a pronounced antenna enhancement around 52 THz (5.7 μ m), which shows enhancement due to the spectral selectivity of the antenna. In this context, the free spectral range (FSR) of the cavity, defined by FSR = $\frac{c}{2\pi L}$, becomes evident. Fig. 4b shows that peaks of the 5.5 μ m TECNA under cross-polarization align well with a linear trend, indicating the cavity as the primary contributor to these multiple peaks. The observed FSR, approximately 51 THz, corresponds to a cavity length near 3 μ m, which is consistent with the fact that effective cavity length ranges between its height (2.5 μ m) and its radius (3.9 μ m).

Upon examining the peak positions in Fig. 4b from measurements using unpolarized light (glowbar) for the 5.5 μm TECNA design, a noticeable deviation from linearity in the blue curve is evident. In contrast, the orange curve, representing the same TECNA under cross-polarization, adheres more closely to a linear trajectory. This difference can be explained as arising from the difference in resonant frequency of the nanoantenna and the cavity. The blue curve for the 5.5 μm TECNA distinctly shows a tail to the right of the main peak (Fig. 3), while the 10.6 μm TECNA exhibits a tail to the left of its main peak. For the 14 μm design, this tail is observed to the left of the rightmost main peak. These tails are indicative of the cavity modes. However, because the antenna's resonant frequency does not perfectly align with these peaks, the maximum is instead located elsewhere. By aligning the peak of the antenna response more closely with the tails, the curves would follow a more linear trajectory. Our prior research [29] has emphasized the

potential of modulating the antenna length for achieving wavelength selectivity, highlighting the nanoantenna's design and geometry's role in enhancing the spectral response, ensuring spectral selectivity, and maintaining consistent polarization characteristics.

While our measurements are in fairly good agreement with our simulations, this approach has some limitations. For example, the calibration of the TECNA's response using the internal DTGS detector is pivotal in our measurements but is not completely known. The reference values [28] for the DTGS might not align with our detector's actual performance due to factors like aging and window material. Such variations emphasize the challenges in determining an exact detectivity, potentially introducing minor calibration errors. Additionally, while providing a general spectral overview, the FTIR resolution, set at 128 cm⁻¹, might not capture the TECNA response's finer details. This broader resolution averages spectral features, resulting in observed peaks that could be wider and have reduced peak heights. Such nuances might account for the slight differences seen in Table 2 between the HFSS simulation and measurement results.

Another limitation in our study is the reliance on metallic materials. Our previous work has demonstrated that Ni/Pd thermocouples exhibit relatively high Seebeck coefficients among metals [10]. In contrast, materials such as Sb_2Te_3 and Bi_2Te_3 offer higher Seebeck coefficients. However, these materials introduce complexities in the fabrication process, particularly when creating nano-scale, free-standing structures. Their brittleness [30], compared to metals, necessitates more sophisticated fabrication methods such as molecular beam epitaxy, sputtering, or chemical vapor deposition for thin films or nanostructures [31]. Despite these challenges, exploring the use of Sb_2Te_3 and Bi_2Te_3 in future research remains promising due to their superior thermoelectric properties.

Although this system relies on the Seebeck effect, the confinement of the field in the junction provided by this geometry (50 nm \times 50 nm \times 50 nm) has significant potential for the creation of other novel detectors. For example, other detecting materials could in principle, be inserted into the system where the junction currently is, which could enhance the antenna's response. This could include microbolometers (which typically employ materials such as VOx [32] or titanium [33] that exhibit significant resistance changes with temperature variations), or QWIPs (which use band-structure engineering to achieve tunable spectral selectivity [34], high quantum efficiency, and high speed [35]). By integrating these materials and technologies within the metallic components of the nanoantenna, for example, using a double-metal bonding process [36], there is potential to increase its sensitivity, extend its spectral range, and achieve better overall performance. Such an integration would also reduce the need for arrays to improve the sensitivity. Consequently, device dimensions could be reduced from the current ~ 100 mm needed for a single array, suggesting possibilities for more compact and efficient infrared detectors in future applications. Alternatively, the array geometry could be used to make efficient focal plane arrays.

4. Conclusion

In this study, we performed the first spectral selectivity measurements of TECNA arrays, demonstrating their capabilities as spectrally-tailored detectors. We showed that the response of the TECNAs comes from a combination of both their antenna properties and their cavity properties. The close agreement between our simulations and experimental results, particularly for the 5.5 μm , 10.6 μm , and 14 μm designs, attests to the reliability and effectiveness of the TECNA design. The distinct spectral selectivity demonstrated by the TECNAs indicates their significant potential in advancing MWIR and LWIR photonics. Such detectors could play a role in chip-scale sensing applications requiring moderate sensitivity and high speed.

CRediT authorship contribution statement

Chao Dong: Data curation, Formal analysis, Investigation, Writing – original draft. Gergo P. Szakmany: Formal analysis, Investigation, Methodology, Writing – review & editing. Hadrian Aquino: Investigation. Wolfgang Porod: Supervision. Alexei O. Orlov: Supervision. Edward C. Kinzel: Formal analysis, Software. Gary H. Bernstein: Funding acquisition, Methodology, Supervision. David Burghoff: Funding acquisition, Investigation, Methodology, Supervision, Writing – review & editing.

Declaration of Competing Interest

The authors declare that they have no known competing financial interests or personal relationships that could have appeared to influence the work reported in this paper.

Data availability

The datasets and accompanying code utilized in this study can be accessed on Figshare under the identifier 10.6084/m9. figshare.24265765.

Acknowledgments

This work was supported by NASA HESTO under grant 19-HTIDS19–0008. It was also funded in part by AFOSR grant no. FA9550–20–1–0192, the Gordon and Betty Moore Foundation through Grant GBMF11446, ONR grant N00014–21–1–2735, and NSF grant ECCS-2046772.

References

- H. Kaplan, Practical applications of infrared thermal sensing and imaging equipment, vol. 75, SPIE Press, 2007.
- [2] M. Vollmer, K.-P. Möllmann, Infrared Thermal Imaging: Fundamentals, Research and Applications, John Wiley & Sons, 2017.
- [3] G.C. Holst, K.A. Krapels, G. Bernstein, R.G. Driggers, Infrared imaging systems: Design, analysis, modeling, testing xx, Opt. Eng. 48 (9) (2009) 093602.
- [4] A. Barh, P. Tidemand-Lichtenberg, C. Pedersen, Thermal noise in mid-infrared broadband upconversion detectors, Opt. Express 26 (3) (2018) 3249–3259.
- [5] S.D. Gunapala, S.V. Bandara, C.J. Hill, D.Z. Ting, J.K. Liu, B. Rafol, E. R. Blazejewski, J.M. Mumolo, S.A. Keo, S. Krishna, et al., 640 × 512 pixels long-wavelength infrared (lwir) quantum-dot infrared photodetector (qdip) imaging focal plane array, IEEE J. Quantum Electron. 43 (3) (2007) 230–237.
- [6] Y. Ma, Y. Chang, B. Dong, J. Wei, W. Liu, C. Lee, Heterogeneously integrated graphene/silicon/halide waveguide photodetectors toward chip-scale zero-bias long-wave infrared spectroscopic sensing, ACS Nano 15 (6) (2021) 10084–10094.
- [7] P.K. Yadav, I. Yadav, B. Ajitha, A. Rajasekar, S. Gupta, Y.A.K. Reddy, Advancements of uncooled infrared microbolometer materials: a review, Sens. Actuators A: Phys. 342 (2022) 113611.
- [8] B. Levine, Quantum-well infrared photodetectors, J. Appl. Phys. 74 (8) (1993) R1–R81.
- [9] C. Fumeaux, M.A. Gritz, I. Codreanu, W.L. Schaich, F.J. González, G.D. Boreman, Measurement of the resonant lengths of infrared dipole antennas, Infrared Phys. Technol. 41 (5) (2000) 271–281.
- [10] G.P. Szakmany, P.M. Krenz, A.O. Orlov, G.H. Bernstein, W. Porod, Antennacoupled nanowire thermocouples for infrared detection, IEEE Trans. Nanotechnol. 12 (2013) 163–167.
- [11] E. Briones, A. Cuadrado, J. Briones, R. Díaz de León, J.C. Martínez-Antón, S. McMurtry, M. Hehn, F. Montaigne, J. Alda, F.J. González, Seebeck nanoantennas for the detection and characterization of infrared radiation, Opt. Express 22 (2014) A1538–A1546.

- [12] G. Szakmany, G. Bernstein, E. Kinzel, A. Orlov, W. Porod, Nanoantenna-based ultrafast thermoelectric long-wave infrared detectors, Sci. Rep. 10 (1) (2020) 1–9.
- [13] A. Rogalski, Infrared detectors: status and trends, Prog. Quantum Electron. 27 (2-3) (2003) 59–210.
- [14] Q. Song, X. Guo, Y. Sun, M. Yang, Anti-solvent precipitation method coupled electrospinning process to produce poorly water-soluble drug-loaded orodispersible films, AAPS PharmSciTech 20 (6) (2019) 246.
- [15] P. Del Haye, A. Schliesser, O. Arcizet, T. Wilken, R. Holzwarth, T. Kippenberg, Optical frequency comb generation from a monolithic microresonator, Nature 450 (2007) 1214–1217.
- [16] A. Griffith, R. Lau, J. Cardenas, Y. Okawachi, A. Mohanty, C. Poitras, A. Gaeta, M. Lipson, Silicon-chip mid-infrared frequency comb generation, Nat. Commun. 5 (2014) 6299.
- [17] M. Yu, Y. Okawachi, A. Griffith, N. Picqué, M. Lipson, A. Gaeta, Silicon-chip-based mid-infrared dual-comb spectroscopy, Nat. Commun. 9 (2016) 1869.
- [18] C. Wang, T. Herr, P. Del'Haye, A. Schliesser, J. Hofer, R. Holzwarth, T.W. Hänsch, N. Picqué, T.J. Kippenberg, Mid-infrared optical frequency combs at 2.5 μm based on crystalline microresonators, Nat. Commun. 4 (2013) 1345.
- [19] D. Burghoff, T. Kao, N. Han, C. Chan, X. Cai, Y. Yang, D. Hayton, J. Gao, et al., Terahertz laser frequency combs, Nat. Photonics 8 (6) (2014) 462–467.
- [20] D. Ren, C. Dong, S.J. Addamane, D. Burghoff, High-quality microresonators in the longwave infrared based on native germanium, Nat. Commun. (2022).
- [21] E. Vicentini, Z. Wang, K. Van Gasse, T.W. Hänsch, N. Picqué, Dual-comb hyperspectral digital holography, Nat. Photonics 15 (2021) 890–894.
- [22] D. Ren, C. Dong, D. Burghoff, Integrated nonlinear photonics in the longwaveinfrared: A roadmap, MRS Commun. (2023) 1–15.
- [23] G.P. Szakmany, A.O. Orlov, G.H. Bernstein, W. Porod, Fabrication of suspended antenna-coupled nanothermocouples, J. Vac. Sci. Technol. B, Nanotechnol. Microelectron.: Mater., Process., Meas., Phenom. 37 (5) (2019) 052201.
- [24] E. Briones, J. Briones, J.C. Martinez-Anton, A. Cuadrado, S. McMurtry, M. Hehn, F. Montaigne, J. Alda, J. González, Seebeck nanoantennas for infrared detection and energy harvesting applications, In: 2015 9th European Conference on Antennas and Propagation (EuCAP), IEEE, 2015, 1-4.
- [25] G.P. Szakmany, A.O. Orlov, G.H. Bernstein, M. Lin, W. Porod, Multiphysics thz antenna simulations, IEEE J. Multiscale Multiphys. Comput. Tech. 3 (2018) 289-294
- [26] G. Szakmany, A. Orlov, G. Bernstein, W. Porod, Cavity-backed antenna-coupled nanothermocouples for infrared detection, In: 2018 IEEE Silicon Nanoelectronics Workshop. 2018.
- [27] G.P. Szakmany, P.M. Krenz, L.C. Schneider, A.O. Orlov, G.H. Bernstein, W. Porod, Nanowire thermocouple characterization platform, IEEE Trans. Nanotechnol. 12 (3) (2013) 309–313.
- [28] K.D. Kempfert, E.Y. Jiang, S. Oas, J. Coffin, Detectors for fourier transform spectroscopy, AN-00125 (2001).
- [29] G.P. Szakmany, G.H. Bernstein, D. Burghoff, D.G. Gonzalez, E.C. Kinzel, A. O. Orlov, W. Porod, D. Strobel, S.M. White, Wavelength selective, polarization sensitive, and uncooled infrared detectors for solar infrared imaging, vol. 11685. Terahertz, RF, Millimeter, and Submillimeter-Wave Technology and Applications XIV, SPIE, 2021, pp. 32–37. vol. 11685.
- [30] B. Huang, G. Li, B. Duan, P. Zhai, W.A. Goddard III, Synergetic evolution of sacrificial bonds and strain-induced defects facilitating large deformation of the bi2te3 semiconductor, ACS Appl. Energy Mater. 3 (3) (2020) 3042–3048.
- [31] E.M. Vieira, J. Figueira, A.L. Pires, J. Grilo, M.F. Silva, A.M. Pereira, L. M. Goncalves, Enhanced thermoelectric properties of sb2te3 and bi2te3 films for flexible thermal sensors, J. Alloy. Compd. 774 (2019) 1102–1116.
- [32] B. Wang, J. Lai, H. Li, H. Hu, S. Chen, Nanostructured vanadium oxide thin film with high tcr at room temperature for microbolometer, Infrared Phys. Technol. 57 (2013) 8–13.
- [33] C. Chen, C. Li, S. Min, Q. Guo, Z. Xia, D. Liu, Z. Ma, F. Xia, Ultrafast silicon nanomembrane microbolometer for long-wavelength infrared light detection, Nano Lett. 21 (19) (2021) 8385–8392.
- [34] X. Nie, H. Zhen, G. Huang, Y. Yin, S. Li, P. Chen, X. Zhou, Y. Mei, W. Lu, Strongly polarized quantum well infrared photodetector with metallic cavity for narrowband wavelength selective detection, Appl. Phys. Lett. 116 (16) (2020).
- [35] D. Palaferri, Y. Todorov, A. Bigioli, A. Mottaghizadeh, D. Gacemi, A. Calabrese, A. Vasanelli, L. Li, A.G. Davies, E.H. Linfield, F. Kapsalidis, M. Beck, J. Faist, C. Sirtori, Room-temperature nine-Mm-wavelength photodetectors and GHz-frequency heterodyne receivers, Nature 556 (7699) (2018) 85–88, 10/gdc6pb.
- [36] B.S. Williams, S. Kumar, H. Callebaut, Q. Hu, J.L. Reno, Terahertz quantum-cascade laser at Λ ≈ 100 Mm using metal waveguide for mode confinement, Appl. Phys. Lett. 83 (11) (2003) 2124–2126, 10/cmgf3n.